Supplementary Material

Table S1. Data collection and refinement statistics.

Crystal	**K1-K10 Heterodimer**
Diffraction Data*	
Space Group	*I* 2 2 2
Unit Cell Dimensions,	
a, *b*, *c* (Å)	75.19, 75.86, 209.29
α, β, γ (°)	90, 90, 90
Resolution range (outer shell), Å	37.37-3.30 (3.38-3.30)†
I/σI	13.76 (0.5)
I/σI at 3.58 Å resolution	1.41
CC(1/2) in outer shell, %	69.6‡
Completeness, %	99.6 (99.4)
R_{meas}	0.073 (4.091)
No. of crystals used	1
No. of unique reflections	9336
Redundancy	6.4 (6.6)
Wilson B-factor, $Å^2$	156.4
Refinement	
R_{work}, %	0.273 (0.471)
R_{free}, %	0.277 (0.482)
No. of Non-Hydrogen Atoms	
Protein	1722
Ligands/Ions	0
Waters	0
R.m.s. Deviations	
Bond lengths, (Å)	0.003
Angles, (°)	0.609
Chirality	0.025
Planarity	0.001
Dihedral, (°)	18.809
Average B-factor (overall), $Å^2$	285.3

* Data collection performed on 06-09-2013.
† Values in parentheses are for highest-resolution (outer) shell.
‡CC* = 1.000; CC_{work} = 0.985; CC_{free} = 0.974.

Table S2. Key residues contributing to the electrostatic surface potential differences between the keratin 1-keratin 10 2B complex and the keratin 5-keratin 14 2B complex.

	K1-K10 2B†	**K5-K14 2B†**
Patch 1	Basic Keratin 1: Arg386, His387, Arg392, Lys395, Arg403, Arg407, Arg 409, Lys416, Lys417	Basic Keratin 5: Lys383, His384, Arg391, Arg395, Arg397 Keratin 10: Arg335, Arg336
Patch 2	Acidic Keratin 10: Glu350, Asp352, Glu356, Glu364, Glu367	Basic Keratin 5: Lys405 Keratin 14: Lys352
Patch 3	Acidic Keratin 1: Glu397, Glu400	Basic Keratin 5: Arg420 Keratin 14: Lys363

†The calculated isoelectric points (pI) for each 2B domain are: K1, 4.99; K5, 5.51; K10, 4.42; K14, 4.59.

Table S3. Distribution of missense mutations in human keratinopathies and identification of specific keratin 1 and keratin 10 helix 2B mutations identified from human patients with skin disease.

I. Distribution of missense mutations in human keratinopathies							
	Keratin Protein Region‡§						
	Head	**H1A**	**H1B**	**H2A**	**H2B**	**Tail**	**L12**
K1	6	11	2	0	16	0	2
K5	17	29	2	1	23	3	17
K6a	1	15	0	0	14	0	0
K6b	0	0	0	0	2	1	0
K6c	0	0	0	0	1	0	0
K10	0	14	0	0	11	0	0
K14	0	32	2	1	22	0	6
K16	0	13	0	0	2	0	0
K17	2	15	0	0	3	0	0
∑	26	129	6	2	94	4	25

II. K1 and K10 mutations identified from human patients with skin disease§		
	Helix 2B Region	
Skin Disease	**Keratin 1**	**Keratin 10**
Epidermolytic Ichthyosis (formerly EHK or BCIE)¶	*Point*: E478K, E478D, I479F, I479T, T481P, Y482C, L486P, L486R, E489K, E490Q, E490G	*Stop*: C427X, Q434X *Insertion*: K439Q *Point*: K439E, R441P, L442Q, E445K, Q447P, Y449D, R450P, L452P, L453P *Deletion*: Q434
Cyclic Ichthyosis with Epidermolytic Hyperkeratosis	*Point*: E478Q, I479T, L485P, E490K	*Stop*: Q434X, *Insertion*: K439Q *Point*: R422E, I446T, Y449C
Epidermolytic Palmoplantar Keratosis	*Insertion*: Q418-I419 *Point*: I479T	
Diffuse Palmoplantar Keratosis#	*Point*: L437P	
Palmoplantar Keratosis	*Deletion*: A459-Q466	

‡Linkers 1 and 2 do not have any known missense mutations to date. H1A, helix 1A; H1B, helix 1B; H2A, helix 2A; H2B, helix 2B; L12, linker between H1B and H2A.
§Data derived from analysis of the Human Intermediate Filament Database (www.interfil.org) (1-32).

¶EHK, epidermolytic hyperkeratosis; BCIE, bullous congenital ichthyosiform erythroderma
#The primary article (2) does not provide histological evidence for either epidermolytic or non-epidermolytic palmoplantar keratoderma (PPK). The L437P^{K1} mutation is incorrectly listed in the Human Intermediate Filament Database as causing non-epidermolytic PPK.

1. Hatsell SJ, Eady RA, Wennerstrand L, Dopping-Hepenstal P, Leigh IM, Munro C, et al. Novel splice site mutation in keratin 1 underlies mild epidermolytic palmoplantar keratoderma in three kindreds. J Invest Dermatol. 2001;116(4):606-9.
2. Liu XP, Ling J, Xiong H, Shi XL, Sun X, Pan Q, et al. Mutation L437P in the 2B domain of keratin 1 causes diffuse palmoplantar keratoderma in a Chinese pedigree. J Eur Acad Dermatol Venereol. 2009;23(9):1079-82.
3. Terron-Kwiatkowski A, Paller AS, Compton J, Atherton DJ, McLean WH, Irvine AD. Two cases of primarily palmoplantar keratoderma associated with novel mutations in keratin 1. J Invest Dermatol. 2002;119(4):966-71.
4. Terron-Kwiatkowski A, Terrinoni A, Didona B, Melino G, Atherton DJ, Irvine AD, et al. Atypical epidermolytic palmoplantar keratoderma presentation associated with a mutation in the keratin 1 gene. Br J Dermatol. 2004;150(6):1096-103.
5. Sun XK, Ma LL, Xie YQ, Zhu XJ. Keratin 1 and keratin 10 mutations causing epidermolytic hyperkeratosis in Chinese patients. J Dermatol Sci. 2002;29(3):195-200.
6. Arin MJ, Longley MA, Epstein EH, Rothnagel JA, Roop DR. Identification of a novel mutation in keratin 1 in a family with epidermolytic hyperkeratosis. Exp Dermatol. 2000;9(1):16-9.
7. Müller FB, Huber M, Kinaciyan T, Hausser I, Schaffrath C, Krieg T, et al. A human keratin 10 knockout causes recessive epidermolytic hyperkeratosis. Hum Mol Genet. 2006;15(7):1133-41.
8. Terheyden P, Grimberg G, Hausser I, Rose C, Korge BP, Krieg T, et al. Recessive epidermolytic hyperkeratosis caused by a previously unreported termination codon mutation in the keratin 10 gene. J Invest Dermatol. 2009;129(11):2721-3.
9. Arin MJ, Oji V, Emmert S, Hausser I, Traupe H, Krieg T, et al. Expanding the keratin mutation database: novel and recurrent mutations and genotype-phenotype correlations in 28 patients with epidermolytic ichthyosis. Br J Dermatol. 2011;164(2):442-7.
10. Yang JM, Nam K, Kim HC, Lee JH, Park JK, Wu K, et al. A novel glutamic acid to aspartic acid mutation near the end of the 2B rod domain in the keratin 1 chain in epidermolytic hyperkeratosis. J Invest Dermatol. 1999;112(3):376-9.
11. Tsubota A, Akiyama M, Kanitakis J, Sakai K, Nomura T, Claudy A, et al. Mild recessive bullous congenital ichthyosiform erythroderma due to a previously unidentified homozygous keratin 10 nonsense mutation. J Invest Dermatol. 2008;128(7):1648-52.

12. Sybert VP, Francis JS, Corden LD, Smith LT, Weaver M, Stephens K, et al. Cyclic ichthyosis with epidermolytic hyperkeratosis: A phenotype conferred by mutations in the 2B domain of keratin K1. Am J Hum Genet. 1999;64(3):732-8.
13. Michael EJ, Schneiderman P, Grossman ME, Christiano AM. Epidermolytic hyperkeratosis with polycyclic psoriasiform plaques resulting from a mutation in the keratin 1 gene. Exp Dermatol. 1999;8(6):501-3.
14. Zeng YP, Chai WX, Fang K, Sun QN, Zuo YG. A recurrent missense mutation of keratin 1 gene in a Chinese family with epidermolytic hyperkeratosis (severe palmoplantar hyperkeratosis, type 1). Int J Dermatol. 2012;51(2):182-5.
15. Muramatsu S, Suga Y, Mizuno Y, Hasegawa T, Tsuchihashi H, Matsuba S, et al. A novel threonine to proline mutation in the helix termination motif of keratin 1 in epidermolytic hyperkeratosis with severe palmoplantar hyperkeratosis and contractures of the digits. Br J Dermatol. 2005;152(5):1087-9.
16. Syder AJ, Yu QC, Paller AS, Giudice G, Pearson R, Fuchs E. Genetic mutations in the K1 and K10 genes of patients with epidermolytic hyperkeratosis. Correlation between location and disease severity. J Clin Invest. 1994;93(4):1533-42.
17. Lee DY, Ahn KS, Lee CH, Rho NK, Lee JH, Lee ES, et al. Two novel mutations in the keratin 1 gene in epidermolytic hyperkeratosis. J Invest Dermatol. 2002;119(4):976-7.
18. Osawa R, Akiyama M, Izumi K, Ujiie H, Sakai K, Nemoto-Hasebe I, et al. Extremely severe palmoplantar hyperkeratosis in a generalized epidermolytic hyperkeratosis patient with a keratin 1 gene mutation. J Am Acad Dermatol. 2011;64(5):991-3.
19. Chassaing N, Kanitakis J, Sportich S, Cordier-Alex MP, Titeux M, Calvas P, et al. Generalized epidermolytic hyperkeratosis in two unrelated children from parents with localized linear form, and prenatal diagnosis. J Invest Dermatol. 2006;126(12):2715-7.
20. Rothnagel JA, Dominey AM, Dempsey LD, Longley MA, Greenhalgh DA, Gagne TA, et al. Mutations in the rod domains of keratins 1 and 10 in epidermolytic hyperkeratosis. Science. 1992;257(5073):1128-30.
21. Joh GY, Traupe H, Metze D, Nashan D, Huber M, Hohl D, et al. A novel dinucleotide mutation in keratin 10 in the annular epidermolytic ichthyosis variant of bullous congenital ichthyosiform erythroderma. J Invest Dermatol. 1997;108(3):357-61.
22. Shimomura Y, Sato N, Tomiyama K, Takahashi A, Ito M. A sporadic case of epidermolytic hyperkeratosis caused by a novel point mutation in the keratin 1 gene. Clin Exp Dermatol. 2006;31(2):286-7.
23. Chipev CC, Yang JM, DiGiovanna JJ, Steinert PM, Marekov L, Compton JG, et al. Preferential sites in keratin 10 that are mutated in epidermolytic hyperkeratosis. Am J Hum Genet. 1994;54(2):179-90.
24. Betlloch I, Lucas Costa A, Mataix J, Pérez-Crespo M, Ballester I. Bullous congenital ichthyosiform erythroderma: a sporadic case produced by a new KRT10 gene mutation. Pediatr Dermatol. 2009;26(4):489-91.

25. Suga Y, Duncan KO, Heald PW, Roop DR. A novel helix termination mutation in keratin 10 in annular epidermolytic ichthyosis, a variant of bullous congenital ichthyosiform erythroderma. J Invest Dermatol. 1998;111(6):1220-3.
26. Sheth N, Greenblatt D, McGrath JA. New KRT10 gene mutation underlying the annular variant of bullous congenital ichthyosiform erythroderma with clinical worsening during pregnancy. Br J Dermatol. 2007;157(3):602-4.
27. Makino T, Furuichi M, Asano Y, Shimizu T. Novel mutation of the KRT 10 gene in a Japanese patient with epidermolytic hyperkeratosis. J Dermatol. 2012;39(1):87-9.
28. Kiritsi D, Nanda A, Kohlhase J, Bernhard C, Bruckner-Tuderman L, Happle R, et al. Extensive postzygotic mosaicism for a novel keratin 10 mutation in epidermolytic ichthyosis. Acta Derm Venereol. 2014;94(3):346-8.
29. McLean WH, Morley SM, Higgins C, Bowden PE, White M, Leigh IM, et al. Novel and recurrent mutations in keratin 10 causing bullous congenital ichthyosiform erythroderma. Exp Dermatol. 1999;8(2):120-3.
30. Virtanen M, Gedde-Dahl T, Mörk NJ, Leigh I, Bowden PE, Vahlquist A. Phenotypic/genotypic correlations in patients with epidermolytic hyperkeratosis and the effects of retinoid therapy on keratin expression. Acta Derm Venereol. 2001;81(3):163-70.
31. Virtanen M, Smith SK, Gedde-Dahl T, Vahlquist A, Bowden PE. Splice site and deletion mutations in keratin (KRT1 and KRT10) genes: unusual phenotypic alterations in Scandinavian patients with epidermolytic hyperkeratosis. J Invest Dermatol. 2003;121(5):1013-20.
32. Mirza H, Kumar A, Craiglow BG, Zhou J, Saraceni C, Torbeck R, et al. Mutations Affecting Keratin 10 Surface-Exposed Residues Highlight the Structural Basis of Phenotypic Variation in Epidermolytic Ichthyosis. J Invest Dermatol. 2015;135(12):3041-50.

Table S4. Biochemical alterations to the structure of the K1-K10 heterodimer caused by missense mutations.

Epidermolytic Ichthyosis (formerly EHK or BCIE)	
Mutation	**Structural Impact of Mutation**
E478K^{K1}	Change of local surface potential from negative to positive; perturbation of hydrogen bonding and electrostatic interactions.
E478D^{K1}	Perturbation of hydrogen bonding and electrostatic interactions, but negative surface charge preserved.
I479F^{K1}	Major steric clashes introduced with K10 residues (L442, E445, I446, Y449).
I479T^{K1}	Loss of stabilizing hydrophobic contacts and hydrogen bonding with K10 (as above) and K1 (D476, R483) residues.
T481P^{K1}	Proline ring δ-carbon clashes with E478^{K1} (1.86 Å from carbonyl oxygen), leading to distal helix kinking to relieve clash. This destabilizes C-terminal 2B helix interface.
Y482C^{K1}	Major elimination of hydrophobic contacts due to loss of aromatic ring; also loss of hydrogen bonding with K1 (E478, T481) and K10 (I446, R450) residues.
L486P^{K1}	Loss of stabilizing hydrophobic interactions and hydrogen bonds with K1 (Y482, R483, L485) and K10 (Y449) residues. Proline ring δ-carbon clashes with E487^{K1} (2.0 Å from hydrogen), likely leading to distal helix kinking to relieve clash.
L486R^{K1}	Perturbation of hydrophobic and hydrogen bond interactions and addition of positive surface charge.
E489K^{K1}	Alteration of local surface charge at C-terminus of 2B helix.
K439E^{K10}	Perturbation of hydrophobic contacts from lysine side chain and change of local surface potential from positive to negative.
R441P^{K10}	Loss of positive surface potential; proline ring δ-carbon clashes with I438^{K10} (1.64 Å from carbonyl oxygen), leading to distal helix kinking to relieve clash. This destabilizes C-terminal 2B helix interface.
L442Q^{K10}	Loss of hydrophobic interactions (e.g. with L475^{K1} and I479^{K1}); gain of electrostatic and hydrogen bonding from polar glutamine.
E445K^{K10}	Disruption of hydrogen bond and electrostatic network between E445^{K10} and I479^{K1}, R441^{K10}, Y449^{K10}. Change from negative to positive surface potential.
Q447P^{K10}	Loss of hydrogen bonding with R450^{K10}. Proline ring γ- and δ-carbons clash with Cα hydrogen (1.9 Å) and carbonyl oxygen (2.0 Å) of N444^{K10}, leading to distal helix kinking. This destabilizes C-terminal 2B helix interface.
Y449D^{K10}	Loss of aromatic ring eliminates stabilizing hydrophobic contacts, especially with Y482^{K1}. Introduction of a negative local surface potential.
R450P^{K10}	Loss of positive local surface charge. Proline ring γ-carbon clashes with carbonyl oxygen (2.1 Å) of Q447^{K10}, leading to distal helix kinking.
L452P^{K10}	Loss of surface-exposed hydrophobic residue. Proline ring δ-carbon may clash with carbonyl oxygen (2.2 Å) of Y449^{K10}, creating distal helix kinking.
L453P^{K10}	Loss of major hydrophobic interaction with L485^{K1}. Proline ring δ-carbon clashes with carbonyl oxygen (1.96 Å) of R450^{K10}, leading to distal helix kinking.
Cyclic Ichthyosis with Epidermolytic Hyperkeratosis	
Mutation	**Structural Impact of Mutation**
E478Q^{K1}	Loss of negative local surface potential; perturbation of hydrogen bonding and electrostatic interactions.
I479T^{K1}	Loss of stabilizing hydrophobic contacts and hydrogen bonding with K10 and K1 residues (as above).
L485P^{K1}	Elimination of hydrophobic interaction (L453^{K10}) and generation of proline ring γ- and δ-carbon clashes with carbonyl oxygen (1.68 Å) of Y482^{K1}, leading to distal helix kinking. This destabilizes C-terminal 2B helix interface.

R422E^{K10}	Loss of contacts with A454^{K1} and L418^{K10}. Change from positive to negative surface charge.
I446T^{K10}	Loss of multiple hydrophobic interactions with K1 (L475, E478, I479, Y482) and K10 (L442, Y449) residues. Loss of hydrogen bonding with E443^{K10}.
Y449C^{K10}	Loss of aromatic ring eliminates stabilizing hydrophobic contacts, especially with Y482^{K1}.
Epidermolytic Palmoplantar Keratosis	
Mutation	**Structural Impact of Mutation**
I479T^{K1}	Loss of stabilizing hydrophobic contacts and hydrogen bonding with K10 and K1 residues (as above).
Diffuse Palmoplantar Keratosis	
Mutation	**Structural Impact of Mutation**
L437P^{K1}	Loss of hydrophobic interactions with Y400^{K10}, Q403^{K10}, and L404^{K10}. Loss of hydrogen bonds with Q403^{K10}. Proline ring γ- and δ-carbon clashes with carbonyl oxygen (1.67-1.69 Å) of E434^{K1}, leading to distal helix kinking. This destabilizes the 2B helix interface.

XDS Data Processing Statistics

```
******************************************************************************
DEFINITIONS:
R-FACTOR
observed = (SUM(ABS(I(h,i)-I(h))))/(SUM(I(h,i)))
expected = expected R-FACTOR derived from Sigma(I)

COMPARED = number of reflections used for calculating R-FACTOR
I/SIGMA  = mean of intensity/Sigma(I) of unique reflections
           (after merging symmetry-related observations)
Sigma(I) = standard deviation of reflection intensity I
           estimated from sample statistics

R-meas   = redundancy independent R-factor (intensities)
           Diederichs & Karplus (1997), Nature Struct. Biol. 4, 269-275.

CC(1/2)  = percentage of correlation between intensities from
           random half-datasets. Correlation significant at
           the 0.1% level is marked by an asterisk.
           Karplus & Diederichs (2012), Science 336, 1030-33
Anomal   = percentage of correlation between random half-sets
 Corr      of anomalous intensity differences. Correlation
           significant at the 0.1% level is marked.
SigAno   = mean anomalous difference in units of its estimated
           standard deviation (|F(+)-F(-)|/Sigma). F(+), F(-)
           are structure factor estimates obtained from the
           merged intensity observations in each parity class.
 Nano    = Number of unique reflections used to calculate
           Anomal_Corr & SigAno. At least two observations
           for each (+ and -) parity are required.
```

SUBSET OF INTENSITY DATA WITH SIGNAL/NOISE >= -3.0 AS FUNCTION OF RESOLUTION

RESOLUTION LIMIT	NUMBER OF REFLECTIONS OBSERVED	UNIQUE	POSSIBLE	COMPLETENESS OF DATA	R-FACTOR observed	R-FACTOR expected	COMPARED	I/SIGMA	R-meas	CC(1/2)	Anomal Corr	SigAno	Nano
14.76	622	121	131	92.4%	2.3%	2.7%	620	57.58	2.6%	100.0*	30	0.849	61
10.44	1253	217	217	100.0%	2.0%	2.8%	1253	59.02	2.2%	100.0*	12	0.833	144
8.52	1562	263	263	100.0%	2.2%	2.8%	1561	55.78	2.5%	99.9*	9	0.932	192
7.38	1914	306	306	100.0%	2.6%	3.1%	1912	44.65	2.8%	100.0*	-3	0.780	227
6.60	2131	342	343	99.7%	4.2%	4.5%	2130	33.34	4.6%	99.9*	3	0.837	267
6.02	2368	382	382	100.0%	7.9%	8.1%	2366	21.10	8.6%	99.7*	1	0.825	305
5.58	2557	403	404	99.8%	12.3%	12.6%	2557	14.34	13.4%	99.6*	-6	0.755	321
5.22	2924	443	443	100.0%	10.0%	10.0%	2924	15.75	10.9%	99.8*	-1	0.801	363
4.92	2857	452	452	100.0%	5.5%	5.3%	2856	23.81	6.0%	99.9*	-7	0.787	372
4.67	3040	469	469	100.0%	6.6%	6.8%	3038	20.38	7.1%	99.9*	-1	0.781	388
4.45	3193	509	509	100.0%	10.6%	10.8%	3192	14.11	11.6%	99.8*	-1	0.774	430
4.26	3496	539	539	100.0%	12.7%	13.1%	3496	12.01	13.9%	99.8*	-2	0.755	448
4.09	3651	550	550	100.0%	17.2%	17.4%	3649	9.08	18.6%	99.8*	0	0.777	459
3.94	3803	562	565	99.5%	30.4%	30.6%	3803	6.12	32.9%	98.8*	3	0.742	487
3.81	3680	592	595	99.5%	53.0%	51.8%	3677	3.53	57.9%	95.3*	0	0.686	492
3.69	3899	596	598	99.7%	64.0%	69.5%	3898	2.42	69.5%	98.4*	4	0.637	500
3.58	3857	622	627	99.2%	136.1%	131.6%	3855	1.41	148.9%	88.2*	3	0.599	522
3.48	4189	649	651	99.7%	198.8%	202.7%	4189	0.87	216.1%	75.3*	3	0.585	553
3.39	4282	658	668	98.5%	269.9%	261.4%	4281	0.66	293.5%	66.6*	1	0.602	564
3.30	4376	662	666	99.4%	377.0%	388.3%	4376	0.47	409.1%	69.6*	-4	0.549	573
total	59654	9337	9378	99.6%	6.7%	7.1%	59633	13.76	7.3%	100.0*	0	0.713	7668

Figure S1. Excerpt from the XDS data processing output file showing several metrics for 20 resolution bins (ranging from 14.76 to 3.30 Å). Reflections were included to 3.30 Å resolution because the CC(1/2) (blue box) in the highest resolution shell is 69% (yellow highlight), well above the 10% significance level. To enable more direct comparison with the K5-K14-2B structure, which was determined utilizing an I/SIGMA cutoff of 1.47 to exclude weaker reflections, the row corresponding to ~ 3.58 Å resolution and I/SIGMA of ~ 1.4 (red box) is highlighted in yellow. Definitions for several of the metrics are listed above as provided by the XDS program.

Additional readings on x-ray statistics:

-Karplus and Diederichs, 2012, Linking crystallographic model and data quality, Science, 336(6084):1030-3.

-Diederichs and Karplus, 2013, Better models by discarding data?, Acta Crystallogr D Biol Crystallogr., 69(7):1215-22.

-Wang and Wing, 2014, Diamonds in the rough: a strong case for the inclusion of weak-intensity X-ray diffraction data. Acta Crystallogr D Biol Crystallogr, 70(5):1491-7.

-Karplus and Diederichs, 2015, Assessing and maximizing data quality in macromolecular crystallography, Curr Opin Struct Biol, 34:60-8.

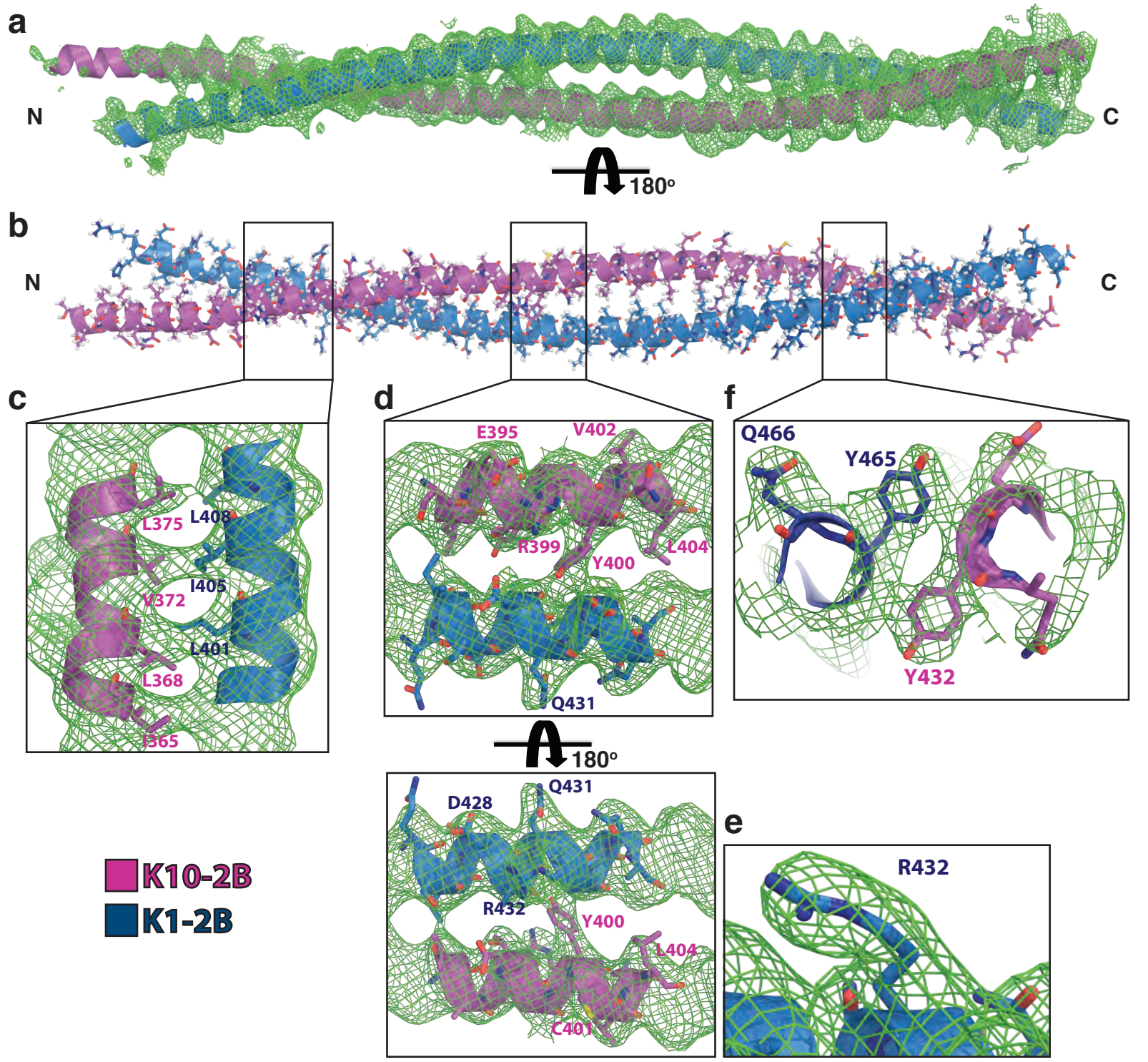

Figure S2. Observed electron density throughout the K1-K10-2B crystal structure. (a) The K1-2B (blue) and K10-2B (magenta) molecules are depicted as ribbons with the electron density (green) for each helix shown. Similar to flexible loops in many proteins, the N-terminus of K10-2B was more flexible (or had more dynamic movement) than other keratin regions in this crystal structure; this is reflected in the weaker electron density at the N-terminus of the K10-2B molecule moreso than the K1-2B molecule. (b) Ribbon diagram of K1-K10-2B heterocomplex with side chains shown in stick format. Three regions are boxed for a higher magnification view in subsequent panels: one from the N-terminus, one from the center, and one from the C-terminus. (c) Close-up view of the observed electron density at the N-terminal aspect of the K1-K10-2B coiled-coil. Hydrophobic residues at the interhelical interface align within the observed density. (d) Close-up views of the observed electron density in the center of the K1-K10-2B coiled-coil, with labeled residues demonstrating good fit within the density. (e) Zoomed in view on K1-2B residue R432 showing it fits well within the observed electron density. (f) Close-up view of the observed electron density at the C-terminal aspect of the K1-K10-2B coiled-coil, particularly around two tyrosine residues, K1-2B-Y465 and K10-2B-Y432. The view in this image is down the coiled-coil long axis. N, N-terminus; C, C-terminus. The electron density in all panels is contoured at 0.8σ.

Multiple Sequence and Structure-based Alignment of Keratins 1 and 10

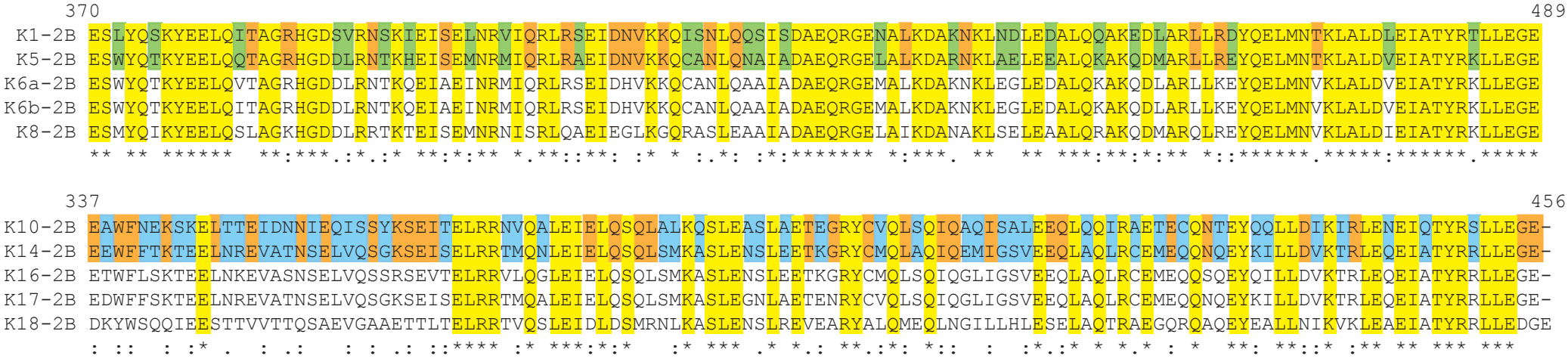

- Residues that are different between K1 and K5 (26 residues different, 94 residues identical; 78% identity)
- Residues that are different between K10 and K14 (46 residues different, 74 residues identical; 62% identity)
- Residues that are conserved between K1 and K5 or K10 and K14, but not across all sequences aligned
- Residues that are conserved across all sequences aligned

Figure S3. Multiple sequence alignment and structure-based alignment of the 2B region of keratins 1 and 10. The multiple sequence alignment calculated by Clustal Omega for the 2B region of keratins 1 and 10 was the same as the structure-based alignment produced by Promals3D comparing K1-2B and K10-2B with K5-2B and K14-2B. Completely conserved residues are denoted by (*). An additional color scheme is illustrated above for the comparison of K1-K10-2B to K5-K14-2B; it highlights residues unique to K1-2B in green and unique to K10 in blue. The numbering above K1-2B represents the initial (370) and last (489) residues in the K1-2B crystallization construct. The numbering above K10-2B represents the initial (337) and last (456) residues in the K10-2B crystallization construct.

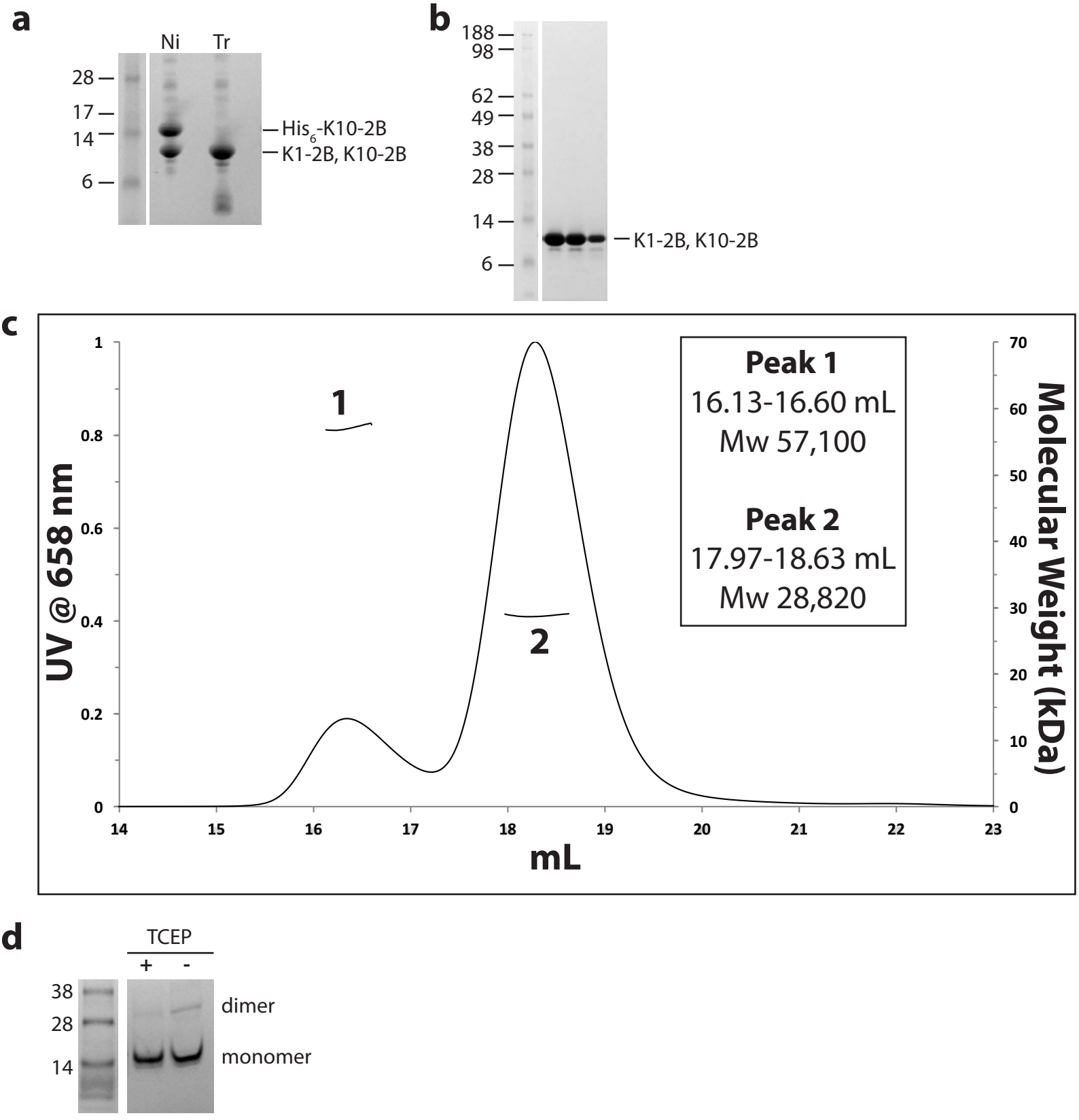

Figure S4. K1-K10-2B purification and biochemical analysis. (a) 4-12% Bis-Tris PAGE showing His_6-K10-2B (calculated MW = 15,950) and K1-2B (calculated MW 13,831) proteins after nickel affinity purification (Ni). After removal of the His-tag from K10 using thrombin, K1-2B and K10-2B (calculated MW = 14,068) migrate similarly (Tr). (b) 4-12% PAGE showing three fractions of purified K1-2B and K10-2B after size exclusion chromatography (SEC). (c) Light scattering of K1-2B/K10-2B complex four days after SEC demonstrated predominantly a homogenous Peak 2 (observed MW 28,820) corresponding to the K1-2B/K10-2B heterodimer (calculated MW = 27, 899). A higher MW Peak 1 (observed MW = 57,100) corresponds to a minor fraction of K1-2B/K10-2B tetramer (calculated MW = 55,798). It likely represents a minor fraction in solution of disulfide-linked heterodimers, given that in panel (d) [non-reducing 3-12% Bis-Tris PAGE] the addition of 10 mM TCEP (a disulfide reducing agent) led to a substantial reduction in the dimer species. Since this was a denaturing gel, the dimer must be held together by a covalent bond; the ability for TCEP to reduce the dimer species suggests there is a disulfide linkage. This is consistent with the observed disulfide bond via $Cys401^{K10}$ in the crystal structure. MW, molecular weight. PAGE, polyacrylamide gel electrophoresis.

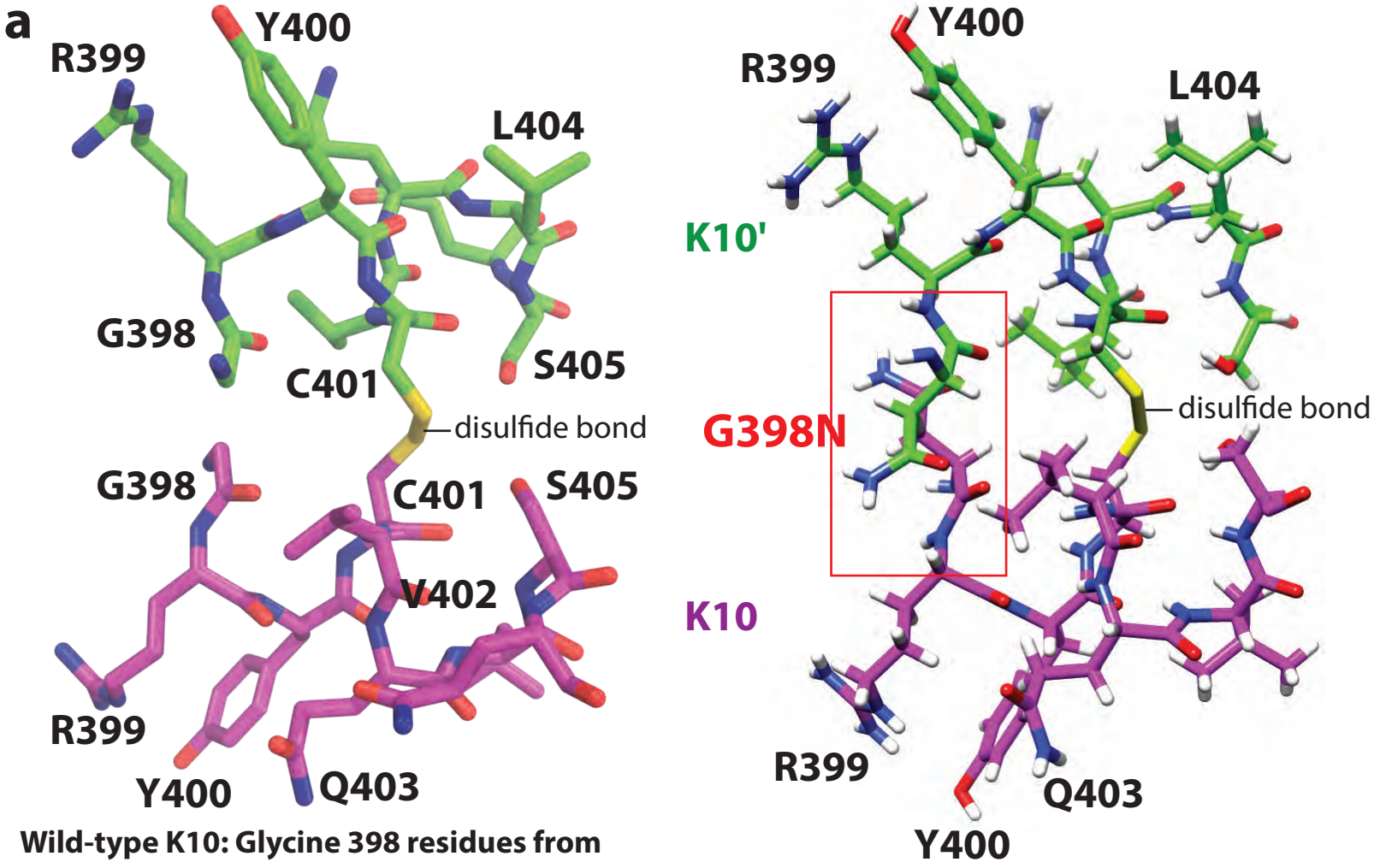
a
Y400
R399
L404
G398
C401
S405
disulfide bond
G398
C401
S405
V402
R399
Y400
Q403
Wild-type K10: Glycine 398 residues from disulfide linked K10 molecules do not clash
Y400
R399
L404
K10'
G398N
disulfide bond
K10
R399
Q403
Y400
Glycine 398K10 mutated to Asn (as present in K17) generates steric clash adjacent to the disulfide linkage
b
K10'
G398N'
disulfide bond
G398N
S405
CLASH
K10

Figure S5

Figure S6. Predicted changes in folding free energy for K10-2B single-site mutations. Using the computer algorithm PoPMuSiC, the change in folding free energy (ΔΔG, kcal/mol) of K10-2B for all possible single-site mutations at each residue position was calculated using as the input structure the disulfide-linked K1-K10-2B heterodimer. ΔΔG values < 0 predict a stabilizing mutation, whereas ΔΔG values > 0 predict destabilizing mutations. The data above depicts the sum of the stabilizing mutations at each residue position; for example, K10-2B residue Gln403 had two predicted stabilizing mutations, Gln-> Leu (-0.16 kcal/mol) and Gln -> Met (-0.08 kcal/mol). This chart shows the sum of this prediction at -0.24 kcal/mol. The black box indicates K10-2B residues 391-405, which make up the longest contiguous stretch in K10-2B having the fewest predicted stabilizing mutations. In other words, this region of K10-2B is less tolerable of mutation and more likely to become destabilized with mutation. For reference, Cys401 is marked with an asterix.

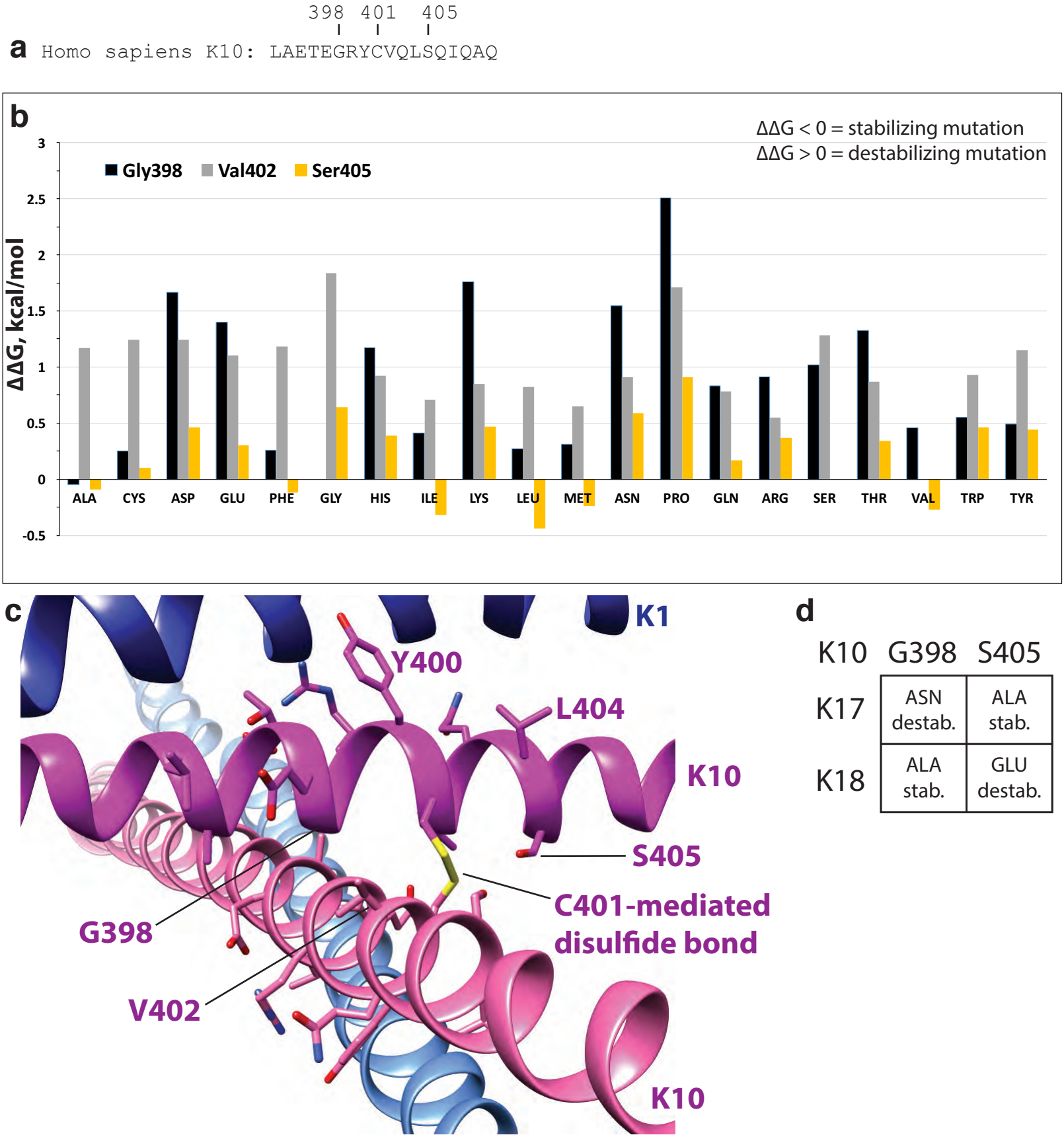

Figure S7. Predicted changes in folding free energy for K10-2B mutations at Gly398, Val402 and Ser405. (a) The amino acid sequence surrounding K10-Cys401. (b) Plot showing the change in folding free energy (ΔΔG, kcal/mol) of the disulfide-linked K1-K10-2B heterodimer when Gly398, Val402 and Ser405 are mutated to all possible other amino acids. For Gly398, one mutation to Ala is predicted to be stabilizing, while all others are destabilizing (black bars). All mutations for Val402 are predicted to be destabilizing (gray bars). Six mutations for Ser405 are predicted to stabilize the structure (yellow bars); these mutations are to hydrophobic residues. (c) Structure of the K1-K10-2B heterodimer around the disulfide site highlighting key residues at the interface. (d) Diagram showing the K17 and K18 residues at equivalent positions to K10-2B 398 and 405. It is also shown whether analysis by PoPMuSiC predicted a K10-2B mutation to the K17 or K18 residue was stabilizing or destabilizing.

Point Mutations Identified in 2B Region of Keratins 1 & 10		
Skin Disease	**Keratin 1**	**Keratin 10**
Epidermolytic Ichthyosis	E478K, E478D, I479F, I479T, T481P, Y482C, L486P, L486R, E489K, E490Q, E490G	K439E, L442Q, E445K, Q447P, Y449D, R450P, L452P, L453P
Cyclic Ichthyosis with Epidermolytic Hyperkeratosis	E478Q, I479T, L485P, E490K	R422E, I446T, Y449C
Epidermolytic Palmoplantar Keratosis	I479T	
Non-Epidermolytic Palmoplantar Keratosis	L437P	

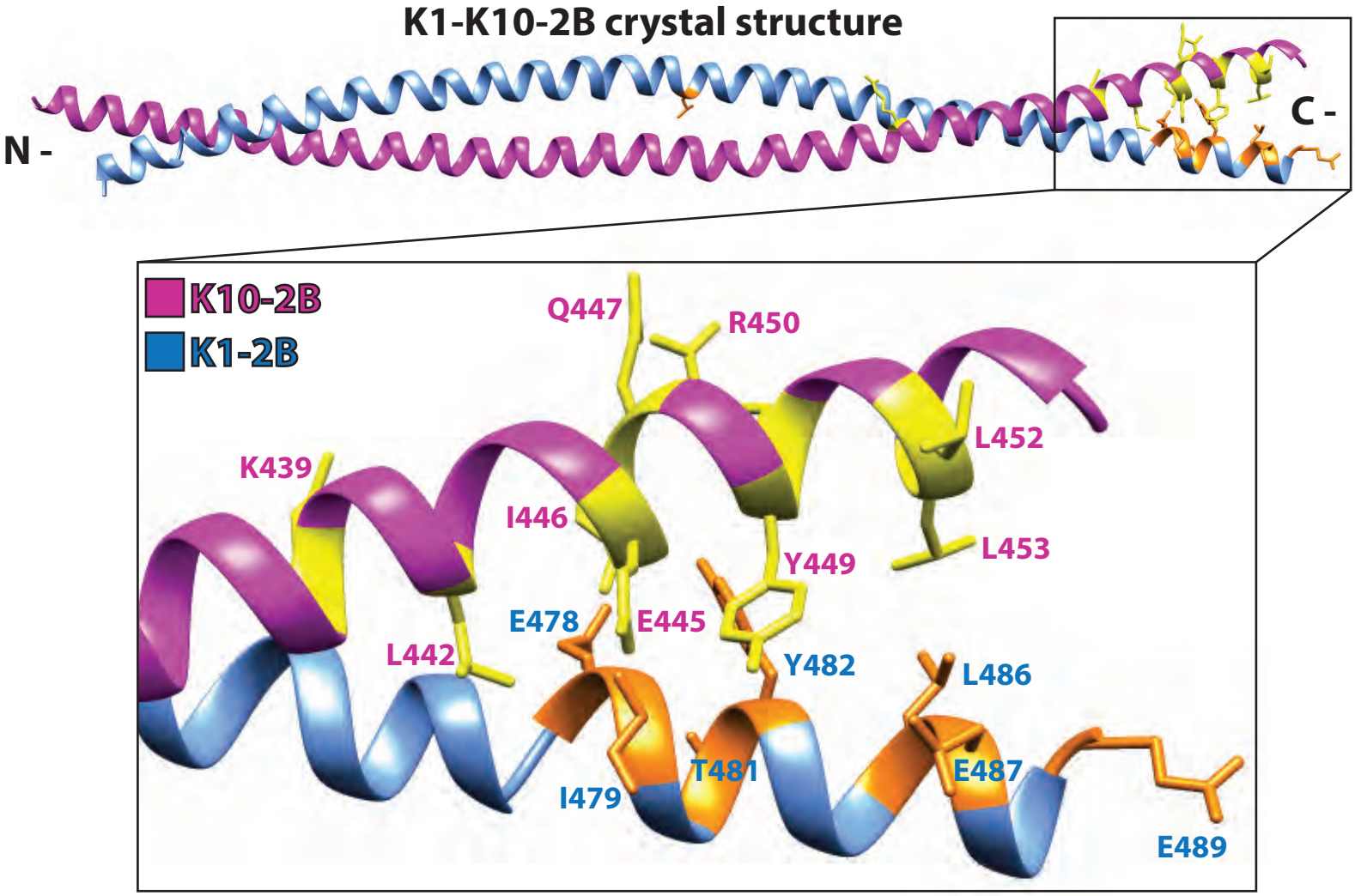

Figure S8. Mapping missense mutations identified in the 2B region of K1 and K10 onto the K1/K10-2B x-ray crystal structure. (Top) Table showing the K1 or K10 missense mutations identified from patients with phenotypic skin disease. The color scheme indicates that K1 will be colored blue, and K10 magenta, in the structure below. Mutations occurring in K1 are colored orange and in K10 colored yellow. (Middle) Full-length K1/K10-2B structure with mutations mapped onto it; a couple mutations exist in the central aspect of the 2B helix, but the majority cluster at the C-terminus. (Bottom) Zoomed in view of the K1/K10 heterodimer C-terminus highlighting the interactions between residues whose mutations lead to K1 or K10 keratinopathies.

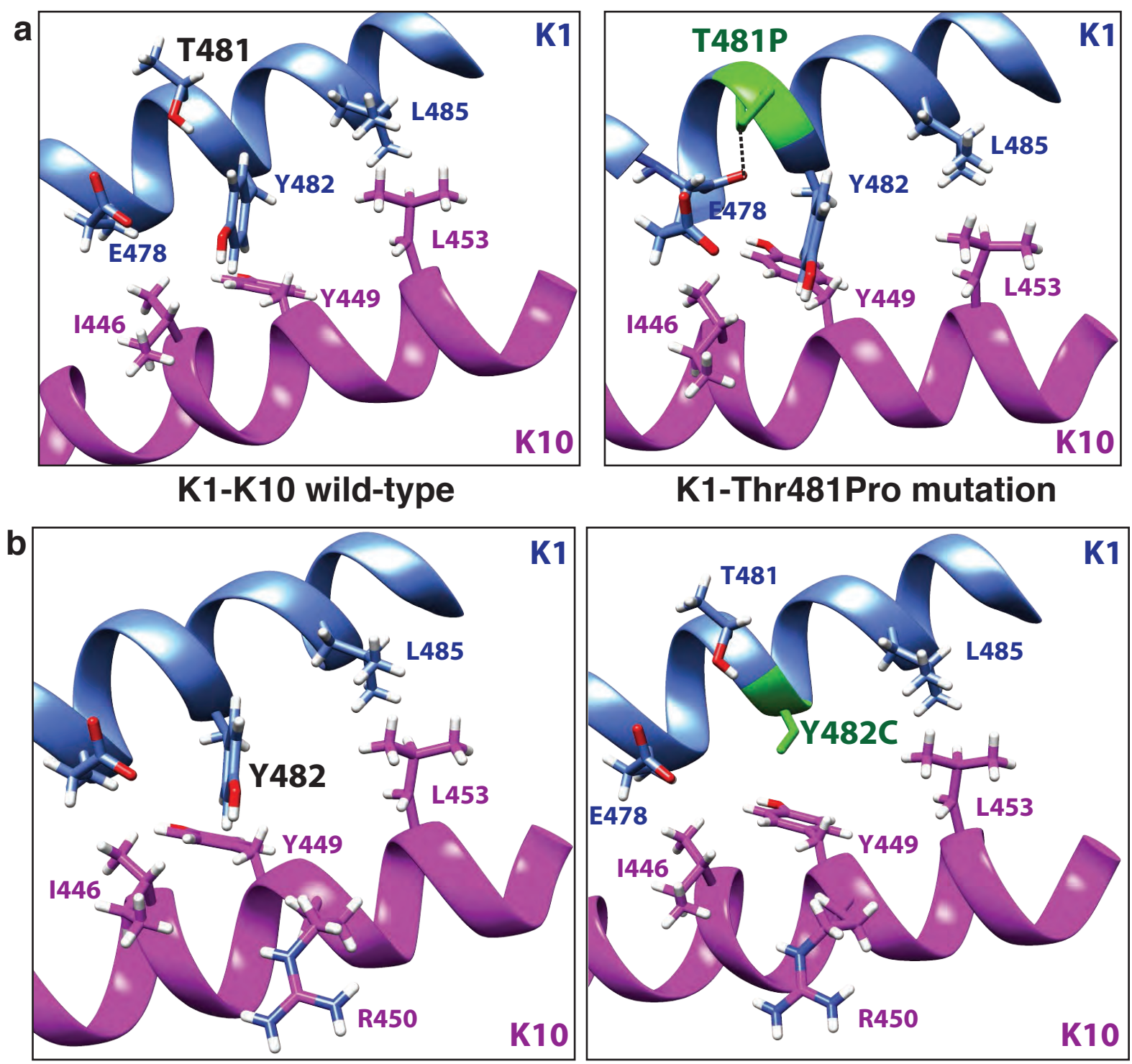
a
T481
K1
L485
Y482
E478
L453
Y449
I446
K10
K1-K10 wild-type
T481P
K1
L485
Y482
E478
L453
Y449
I446
K10
K1-Thr481Pro mutation
b
K1
L485
Y482
L453
Y449
I446
R450
K10
K1-K10 wild-type
T481
K1
L485
Y482C
E478
L453
Y449
I446
R450
K10
K1-Tyr482Cys mutation

Figure S9

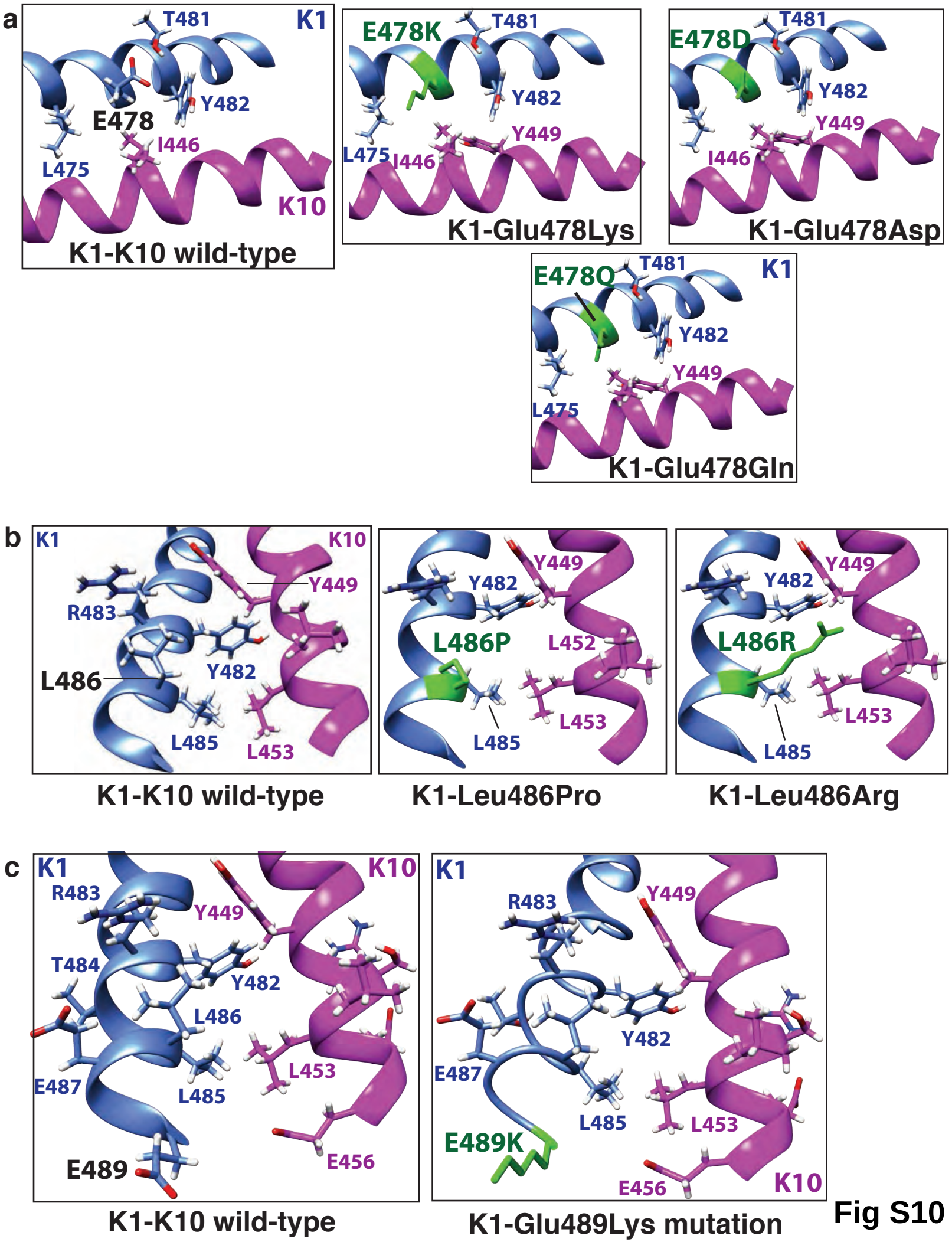
a
T481
K1
E478
Y482
I446
L475
K10
K1-K10 wild-type
E478K
T481
Y482
Y449
L475
I446
K1-Glu478Lys
E478D
T481
Y482
Y449
I446
K1-Glu478Asp
E478Q
T481
K1
Y482
Y449
L475
K1-Glu478Gln
b
K1
K10
Y449
R483
L486
Y482
L485
L453
K1-K10 wild-type
Y449
Y482
L486P
L452
L485
L453
K1-Leu486Pro
Y449
Y482
L486R
L453
L485
K1-Leu486Arg
c
K1
K10
R483
Y449
T484
Y482
L486
E487
L485
L453
E489
E456
K1-K10 wild-type
K1
R483
Y449
Y482
E487
L485
L453
E489K
E456
K10
K1-Glu489Lys mutation

Fig S10

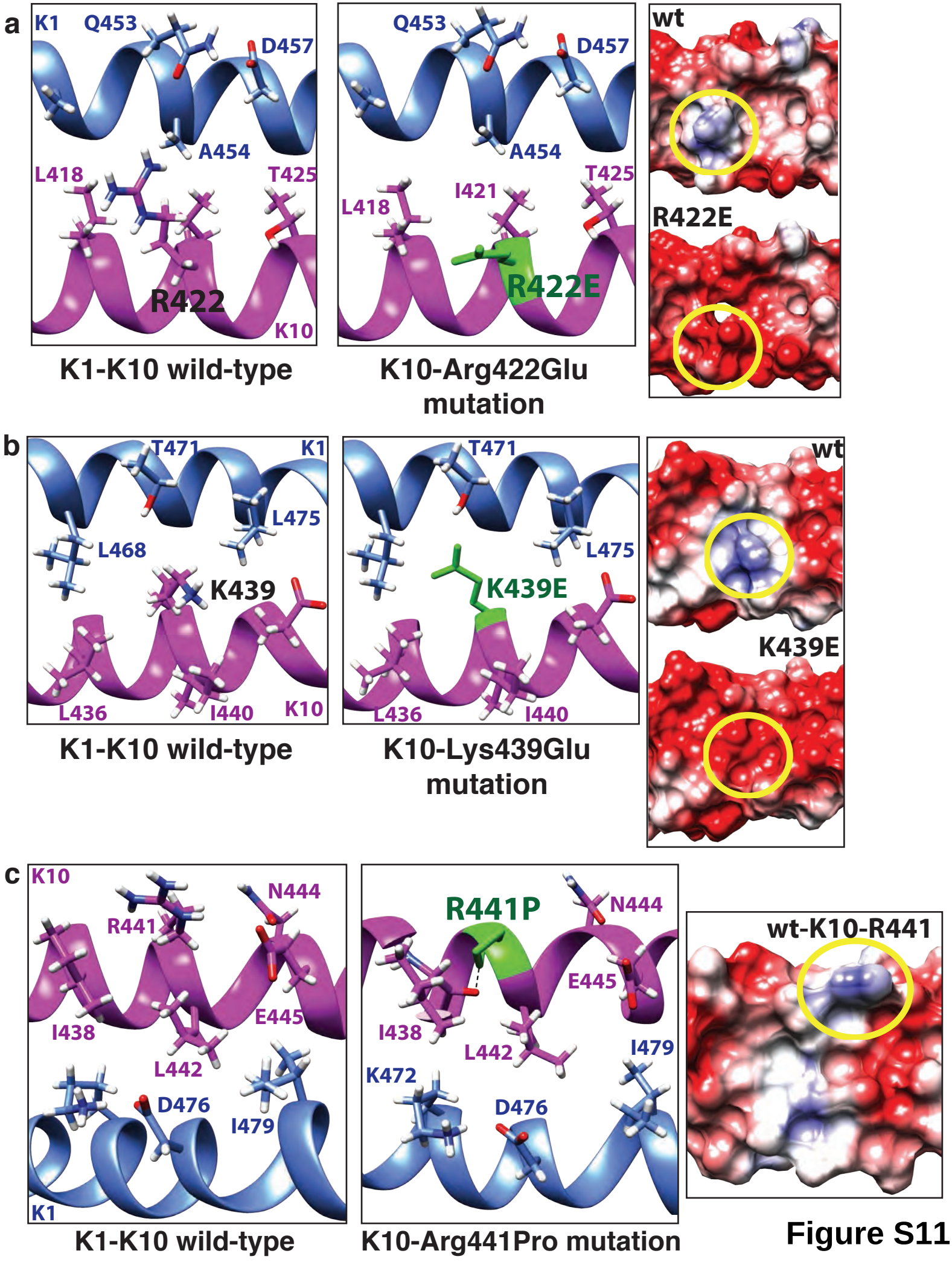
a
K1
Q453
D457
A454
L418
T425
R422
K10
K1-K10 wild-type
Q453
D457
A454
T425
I421
L418
R422E
K10-Arg422Glu mutation
wt
R422E
b
T471
K1
L475
L468
K439
L436
I440
K10
K1-K10 wild-type
T471
L475
K439E
L436
I440
K10-Lys439Glu mutation
wt
K439E
c
K10
N444
R441
E445
I438
L442
D476
I479
K1
K1-K10 wild-type
R441P
N444
E445
I438
L442
I479
K472
D476
K10-Arg441Pro mutation
wt-K10-R441

Figure S11

Figure S12

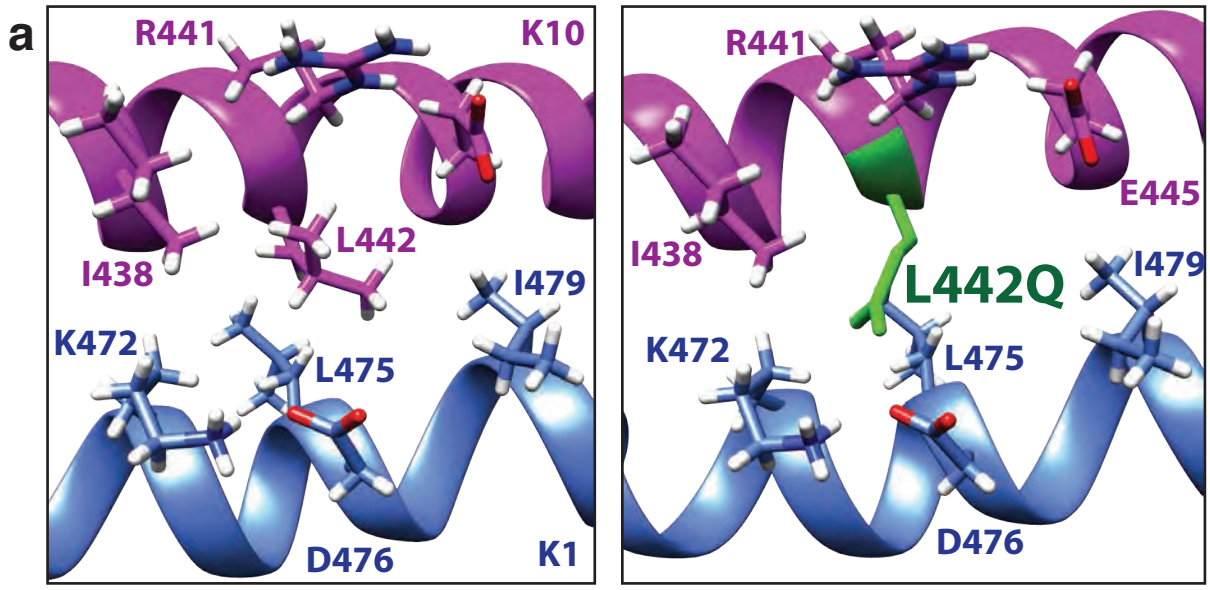

K1-K10 wild-type

K10-Leu442Gln mutation

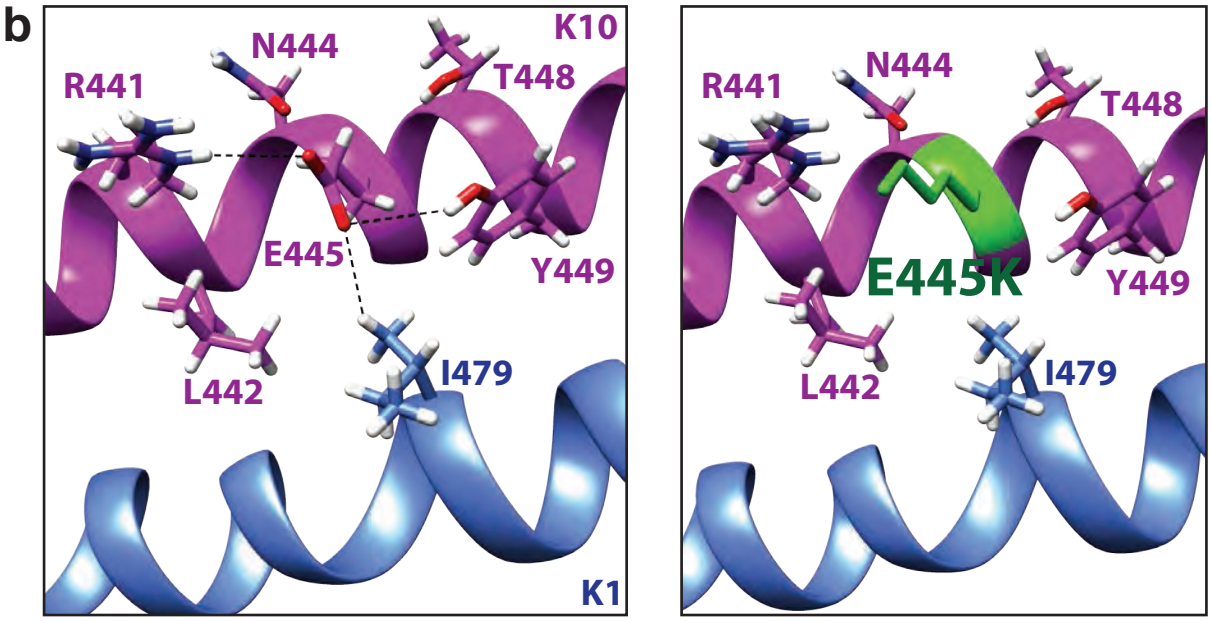

K1-K10 wild-type

K10-Glu445Lys mutation

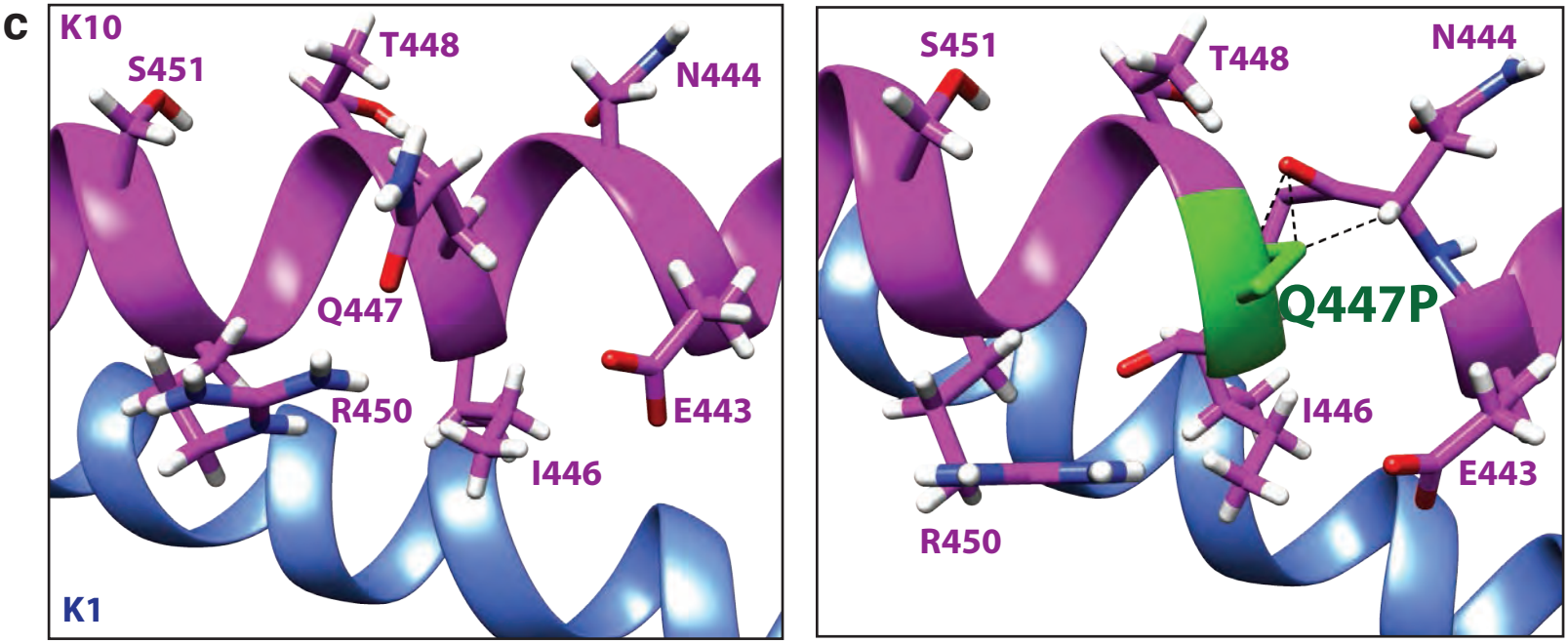

K1-K10 wild-type

K10-Gln447Pro mutation

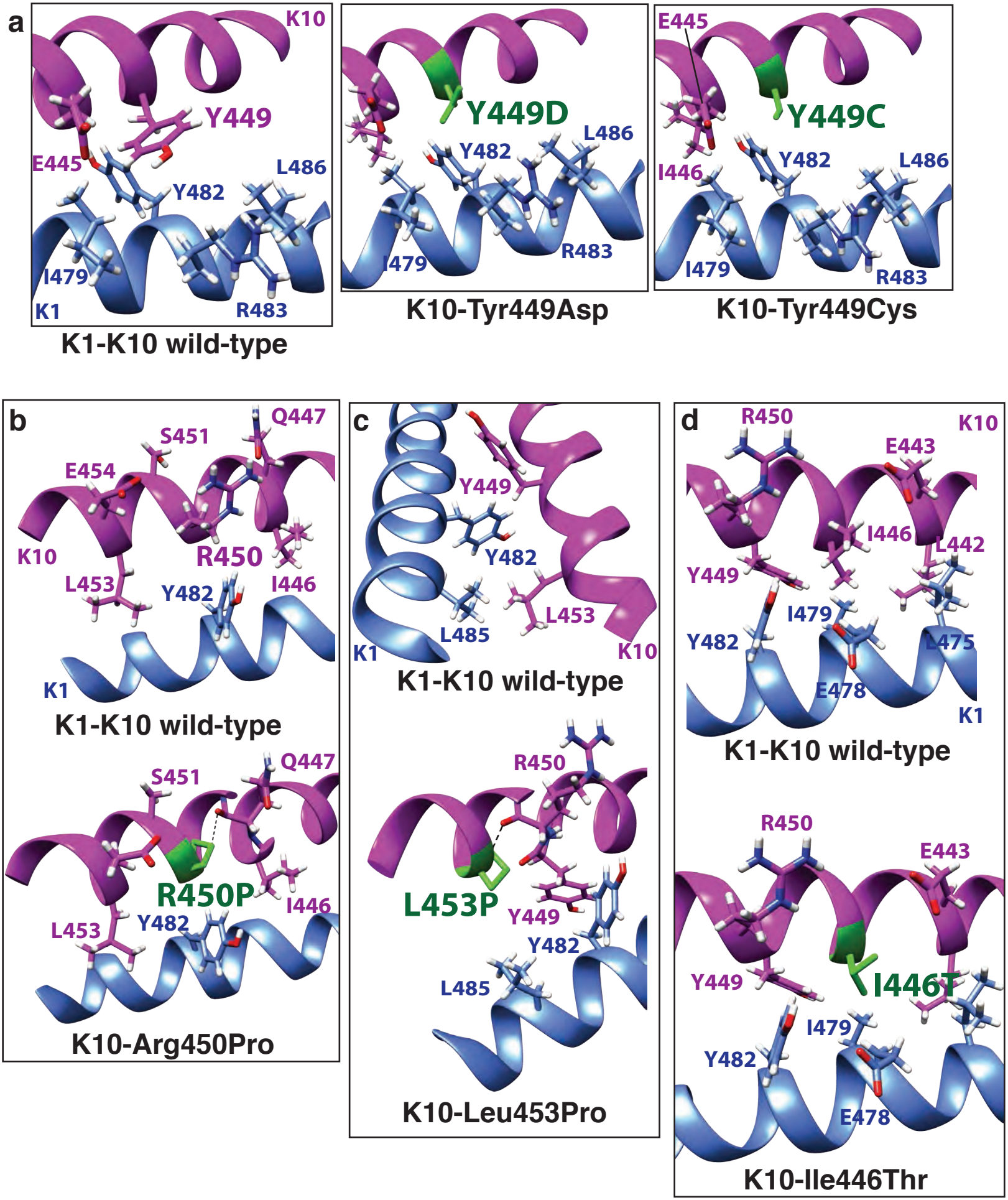
a
K10
Y449
E445
L486
Y482
I479
K1
R483
K1-K10 wild-type
Y449D
L486
Y482
I479
R483
K10-Tyr449Asp
E445
Y449C
I446
Y482
L486
I479
R483
K10-Tyr449Cys
b
Q447
S451
E454
K10
R450
L453
Y482
I446
K1
K1-K10 wild-type
S451
Q447
R450P
I446
L453
Y482
K10-Arg450Pro
c
Y449
Y482
L485
L453
K1
K10
K1-K10 wild-type
R450
L453P
Y449
Y482
L485
K10-Leu453Pro
d
R450
K10
E443
I446
L442
Y449
I479
Y482
L475
E478
K1
K1-K10 wild-type
R450
E443
I446T
Y449
I479
Y482
E478
K10-Ile446Thr

Figure S13

a

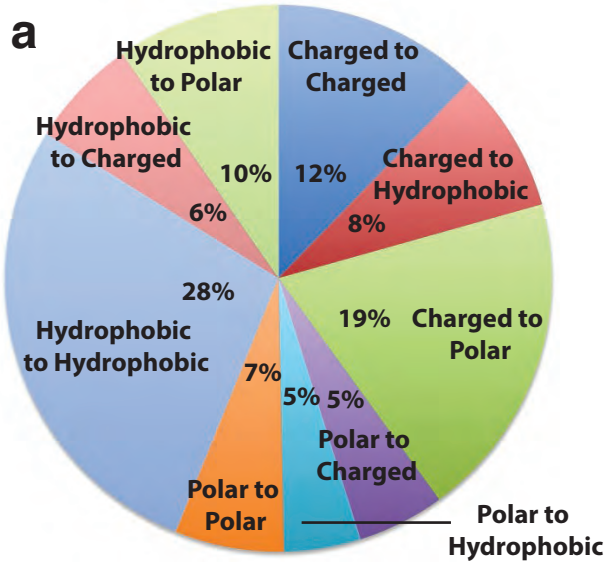

Keratins 5 and 14

b

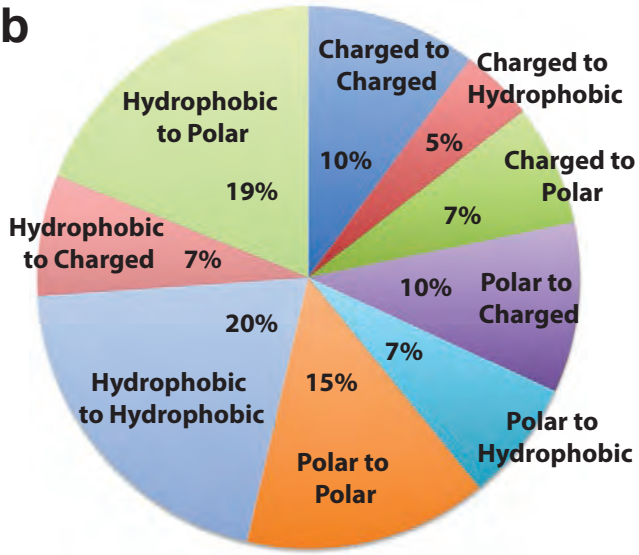

Pachyonychia Congenita Keratins

c

	K1	K10	K5	K14	K6a	K6b	K6c	K16	K17
Positive to Positive	0	0	1	0	0	0	0	0	0
Negative to Negative	1	0	5	0	1	0	0	0	0
Positive to Negative	0	2	2	1	0	0	0	0	0
Positive to Hydrophobic	2	3	3	6	1	0	0	1	1
Positive to Polar	1	4	14	10	0	0	0	2	2
Negative to Positive	3	1	7	3	3	2	1	0	0
Negative to Hydrophobic	1	0	2	2	0	0	0	0	0
Negative to Polar	4	0	5	1	1	0	0	0	0
Polar to Positive	1	0	2	2	1	0	0	0	1
Polar to Negative	0	2	3	1	1	0	0	1	3
Polar to Hydrophobic	4	1	4	3	3	0	0	1	1
Polar to Polar	3	3	5	5	5	1	0	2	2
Hydrophobic to Hydrophobic	12	4	25	18	5	0	0	3	6
Hydrophobic to Positive	1	1	3	1	0	0	0	2	2
Hydrophobic to Negative	1	0	4	2	1	0	0	0	0
Hydrophobic to Polar	3	4	7	8	8	0	0	3	2

	K1	K10	K5	K14	K6a	K6b	K6c	K16	K17
Charged to Charged	4	3	15	4	4	2	1	0	0
Charged to Hydrophobic	3	3	5	8	1	0	0	1	1
Charged to Polar	5	4	19	11	1	0	0	2	2
Polar to Charged	1	2	5	3	2	0	0	1	4
Polar to Hydrophobic	4	1	4	3	3	0	0	1	1
Polar to Polar	3	3	5	5	5	1	0	2	2
Hydrophobic to Hydrophobic	12	4	25	18	5	0	0	3	6
Hydrophobic to Charged	2	1	7	3	1	0	0	2	2
Hydrophobic to Polar	3	4	7	8	8	0	0	3	2

Data derived from analysis of the Human Intermediate Filament Database.

Figure S14

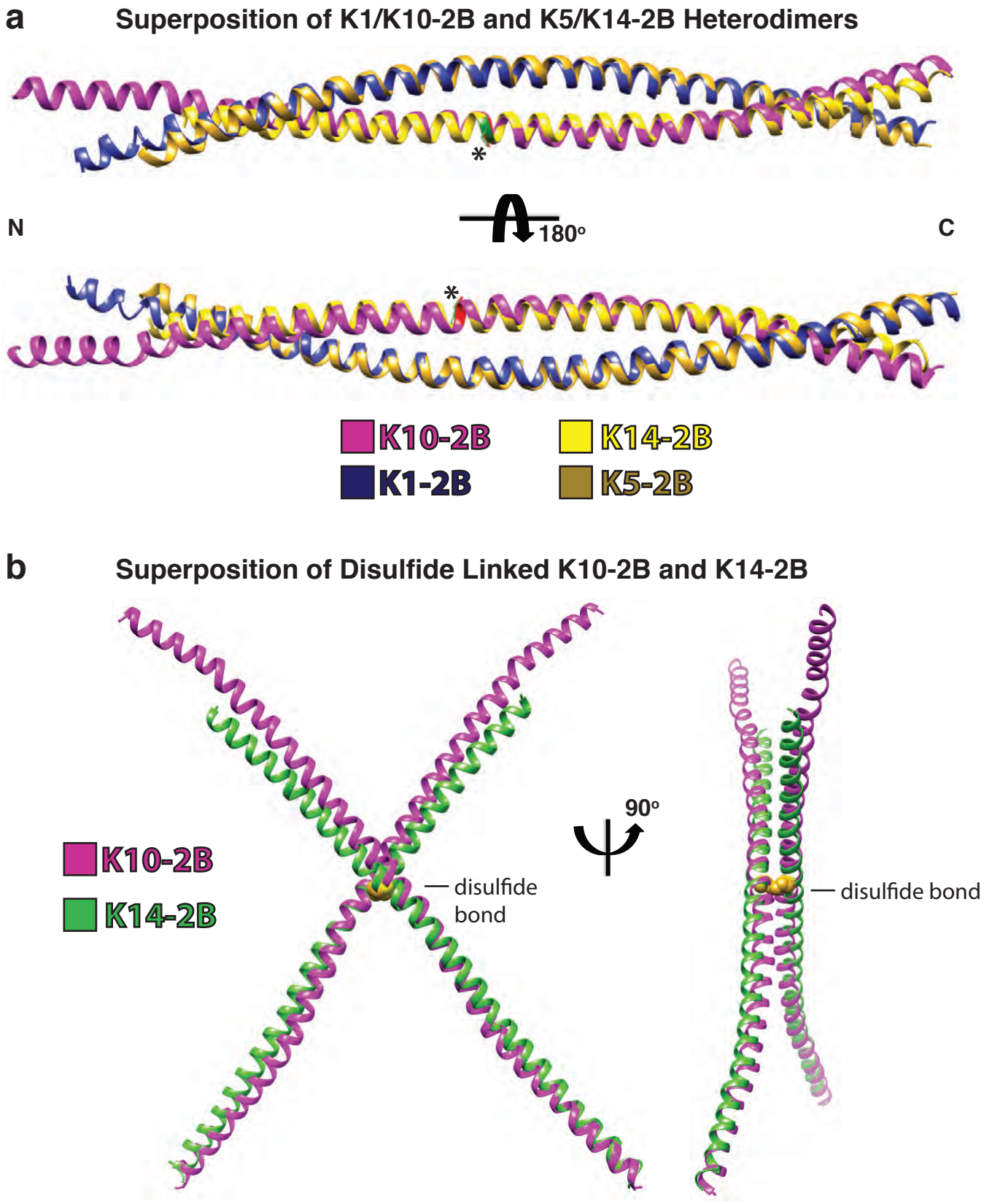

Figure S15. Superposition of the K1/K10-2B structure with K5/K14-2B structure. (a) The K1/K10-2B heterodimer (K1, blue; K10, pink) is presented in ribbon diagram with the K5/K14-2B structure (PDB Code 3TNU; K5, gold; K14, yellow) superimposed using Chimera to highlight subtle differences in helical conformation. The root mean square deviation (RMSD) between the structures is 1.74 Å. Cys401 in K10 (red) and Cys367 in K14 (green) are marked by the asterix. (b) The K10-2B helix (pink) is shown in ribbon diagram disulfide bonded (the disulfide is represented as yellow spheres) to its crystal lattice symmetry mate. The K14-2B helix (green) is shown in ribbon diagram disulfide bonded to its symmetry mate (gold spheres) and superimposed on the K10-2B helix from the K1-K10-2B crystal structure. The K1 and K5 molecules have been omitted for clarity. The RMSD between these disulfide linked structures is 2.49 Å. N, N-terminus; C, C-terminus.

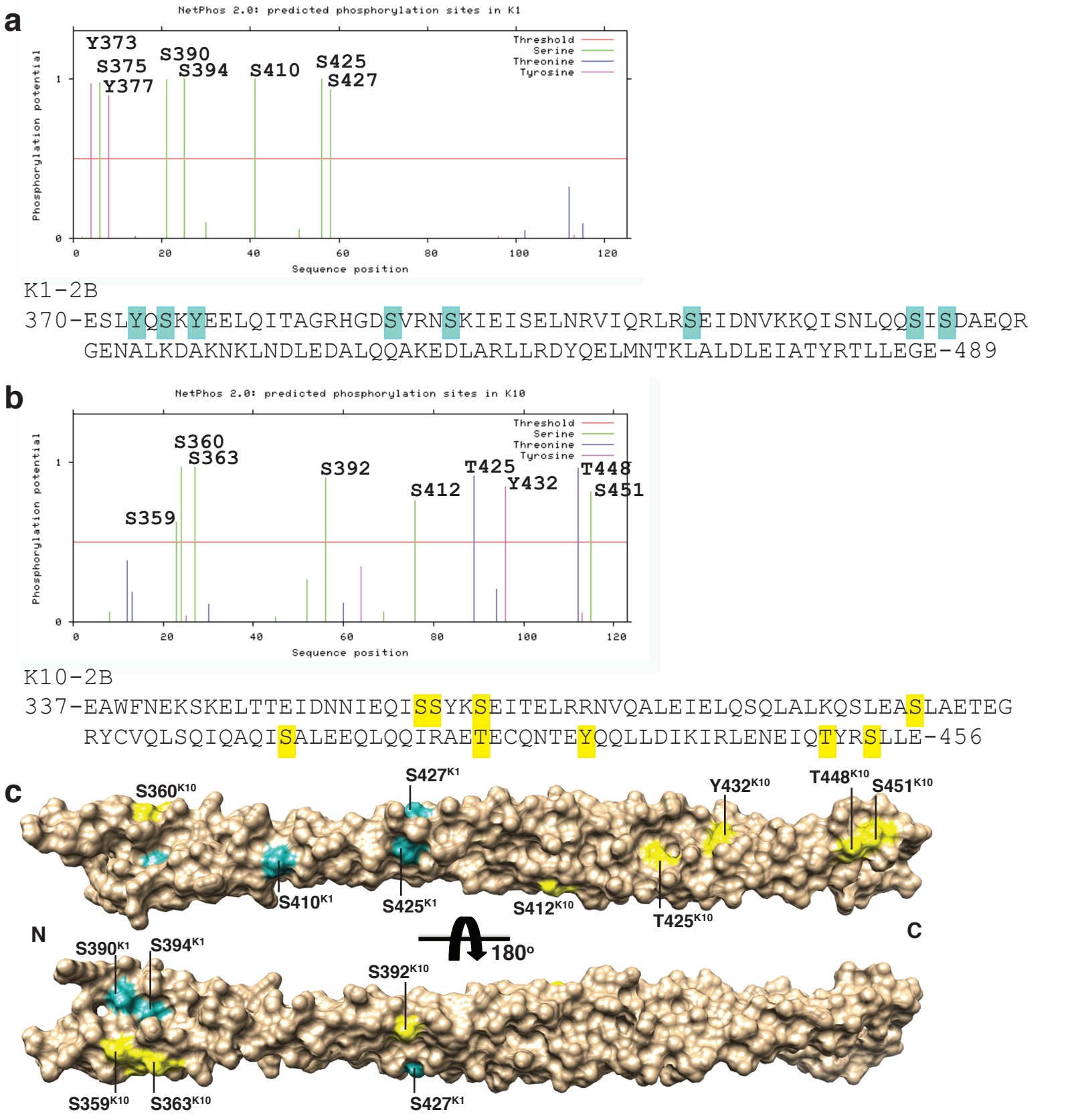

Figure S16. Predicted phosphorylation potential for residues in K1/K10-2B. Using the NetPhos 2.0 Server (at www.expasy.org), phosphorylation potential was calculated for all sequence positions in K1 (a) and K10 (b) and plotted. Eight residues in K1 and nine in K10 scored above threshold (red horizontal line). Below each plot is the corresponding 2B region amino acid sequence, with specific phosphorylation sites scoring above the threshold colored sea-green (K1) or yellow (K10). (c) These residues are mapped onto the molecular surface of the K1/K10-2B crystal structure to indicate the positions of putative phosphorylation sites. Phosphorylation at any of these sites could further alter, and diversify, the surface charge of K1/K10-2B compared to other keratins. [NetPhos reference: Sequence- and structure-based prediction of eukaryotic protein phosphorylation sites. Blom, N., Gammeltoft, S., and Brunak, S. Journal of Molecular Biology: 294(5):1351-1362, 1999].

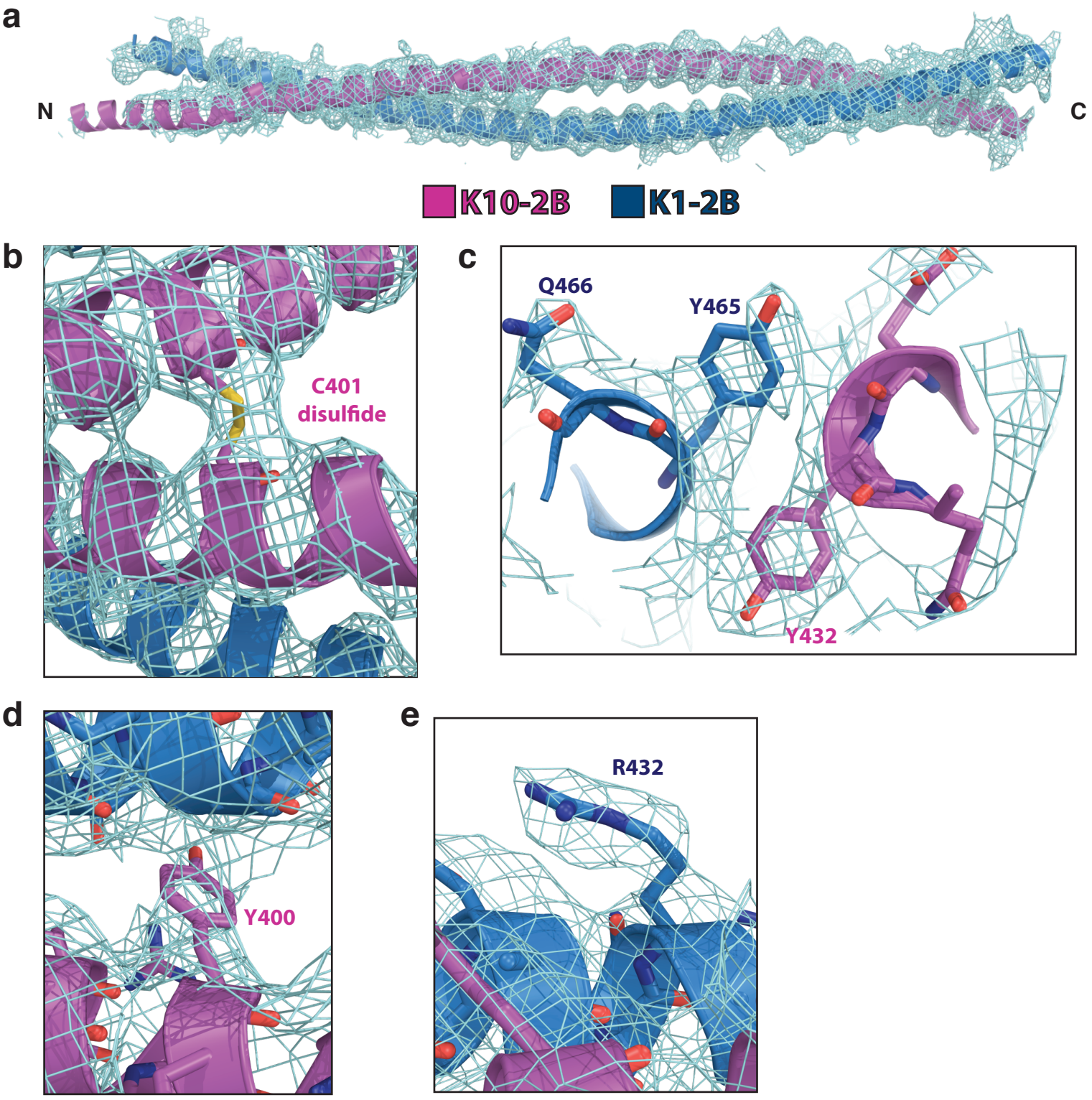

Figure S17. Unbiased simulated annealing composite omit map electron density for the K1-K10-2B crystal structure. (a) The K1-2B (blue) and K10-2B (magenta) molecules are depicted as ribbons with the electron density (cyan) for each helix shown (calculated using PHENIX). Similar to flexible loops in many proteins, the N-terminus of K10-2B was more flexible (or had more dynamic movement) than other keratin regions in this crystal structure, correlating with its weaker electron density. (b) Robust electron density exists at the Cys401^{K10}-mediated disulfide linkage. (c) Close-up view of the unbiased electron density at the C-terminal aspect of the K1-K10-2B coiled-coil, particularly around two tyrosine residues, K1-2B-Y465 and K10-2B-Y432. (d) Close-up view of the unbiased electron density at K10 residue Y400. (e) Zoomed in view on K1-2B residue R432 showing it fits well within the unbiased electron density. N, N-terminus; C, C-terminus. The electron density is contoured at 2.0σ for panel b, and at 0.8σ for the other panels.

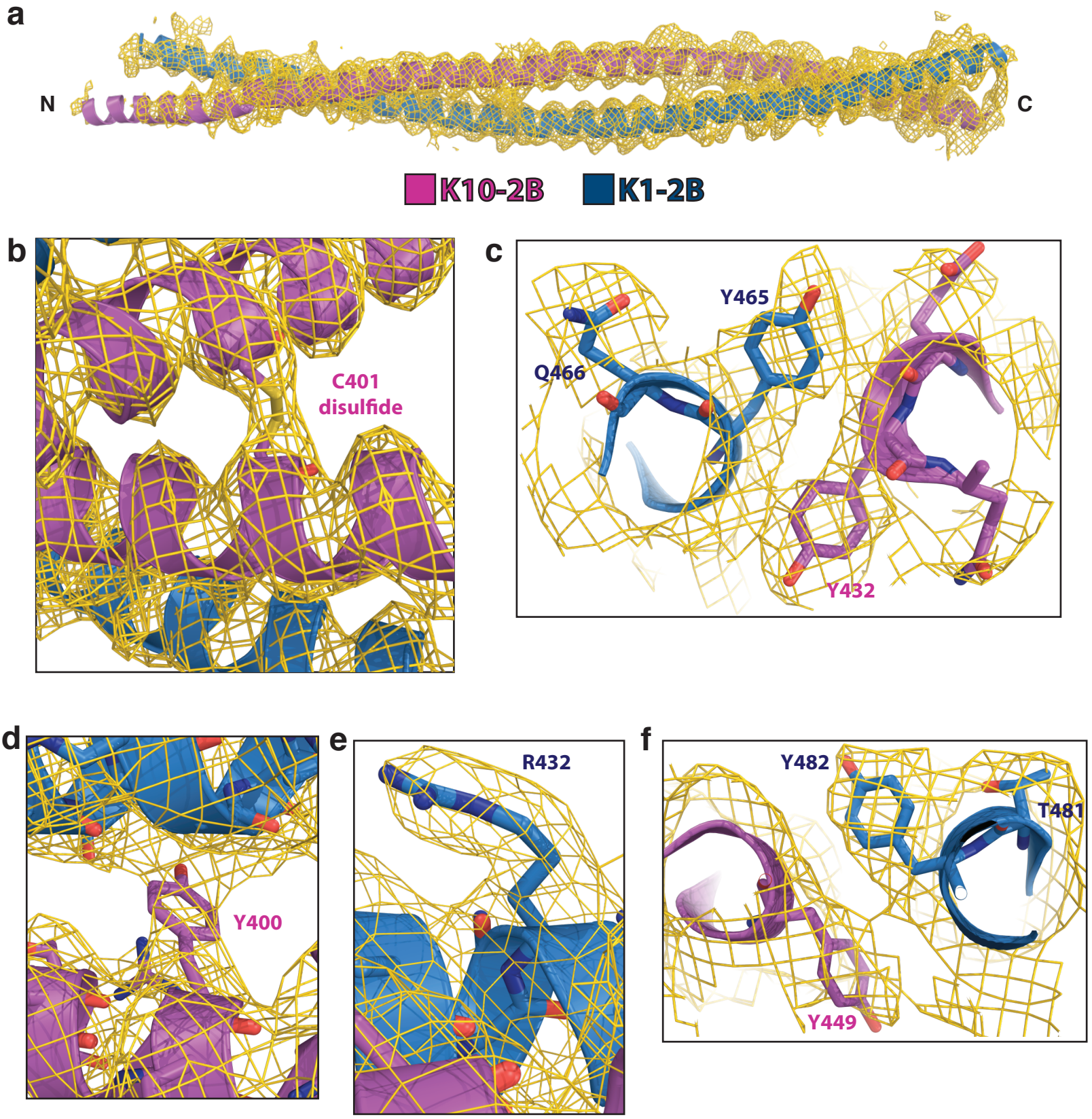

Figure S18. Feature enhanced electron density for the K1-K10-2B crystal structure.
(a) The K1-2B (blue) and K10-2B (magenta) molecules are depicted as ribbons with the feature enhanced electron density (gold) for each helix shown (calculated using PHENIX). (b) Robust electron density exists at the Cys401^{K10}-mediated disulfide linkage. (c) Close-up view of the feature enhanced electron density of two C-terminal tyrosine residues, Y465^{K1} and Y432^{K10}. Close-up views of the feature enhanced electron density of Y400^{K10} (d), R432^{K1} (e), and two additional C-terminal tyrosine residues, Y482^{K1} and Y449^{K10} (f). N, N-terminus; C, C-terminus. The electron density is contoured at 2.0σ for panel b, and at 0.8-1.0σ for the other panels.

Figure Legends for select Supplemental Figures

Fig. S5. Mutation of glycine 398^{K10} to asparagine generates steric clash adjacent to the disulfide bond site. (a) The wild-type K1-K10 2B structure surrounding the disulfide bond site (left) demonstrates appropriate structural stereochemistry and no atomic clashes between adjacent glycine 398 residues. When incorporating a Gly398Asn mutation in K10 computationally, making the 398 position similar to that seen in K17, there is new steric clash between the Asn398 residues (right, within red box). (b) Focused view of Gly398Asn^{K10} rotated 70^{o} about the y-axis compared to panel 'a', showing atomic clash between C_{β} hydrogen atoms.

Fig. S9. Structural consequences of Keratin 1 mutations T481P and Y482C. (a) The left panel shows wild-type T481^{K1} in a relatively surface-exposed position at the distal end of the K1-2B helix. T481P^{K1} mutation (green) introduces a steric clash between the proline ring δ–carbon and the carbonyl oxygen on E478^{K1} (1.86 Å). To relieve this clash, the K1-2B helix must adopt a kinked form. (b) The left panel demonstrates wild-type K1-K10 packing at the distal end of the 2B region, where Y482^{K1} has hydrophobic interactions with Y449^{K10} and I446^{K10} (magenta). Y482C^{K1} mutation (green) disrupts these stabilizing interactions.

Fig. S10. Structural consequences of Keratin 1 mutations E478K, E478D, E478Q, L486P, L486R, and E489K. (a) The left panel demonstrates wild-type K1-K10 packing at the distal end of the 2B helix, where E478^{K1} has electrostatic and hydrogen bond interactions with neighboring residues T481^{K1}, Y482^{K1}, and I446^{K10}. E478K^{K1} mutation (green) disrupts these interactions and causes a negative to positive charge change on the molecular surface. E478D^{K1} and E478Q^{K1} mutations (green) both disrupt the electrostatic and hydrogen bond interactions, but E478D^{K1} preserves the local negative surface charge whereas E478Q^{K1} reduces the negative surface potential. (b) L486P^{K1} and L486R^{K1} mutations (green) cause the loss of stabilizing hydrophobic and hydrogen bond interactions with K1 (Y482, R483, L485) and K10 (Y449) residues. L486P^{K1} mutation also causes the proline ring δ–carbon to clash with E487^{K1}, whereas L486R^{K1} mutation introduces a new positive charge. (c) E489K^{K1} mutation (green) causes alteration of the local surface charge at the C-terminus of helix 2B.

Fig. S11. Structural perturbations caused by Keratin 10 mutations R422E, K439E, and R441P. (a) The left panel shows wild-type R422^{K10} interactions with A454^{K1} and L418^{K10}. R422E^{K10} mutation (green, center panel) disrupts hydrophobic interactions with those two residues, and causes a positive (blue) to negative (red) charge alteration on the molecular surface (right panel). (b) The left panel shows wild-type K439^{K10} has hydrophobic side chain interactions with L468^{K1} and L475^{K1}. K439E^{K10} mutation (green, center panel) reduces these interactions and causes a positive (blue) to negative (red) charge alteration on the molecular surface (right panel). (c) The left and right panels show wild-type R441^{K10} in a surface-exposed location where it forms a positively charged patch (blue). R441P^{K10} mutation (green, center panel) eliminates the positive surface patch and will introduce helix kinking due to the proline ring δ–carbon clashing with the carbonyl oxygen of I438^{K10} (black dashed line).

Fig. S12. Structural perturbations caused by Keratin 10 mutations L442Q, E445K, and Q447P. (a) The left panel shows wild-type L442^{K10} forming hydrophobic interactions with L475^{K1} and I479^{K1}. These interactions are diminished by the L442Q^{K10} mutation (green), with introduction of electrostatic and hydrogen bond interactions from the polar glutamine. (b) Wild-type E445^{K10} forms electrostatic and hydrogen bonds (dashed lines) with I479^{K1}, R441^{K10}, and Y449^{K10}. These interactions are disrupted by E445K^{K10} mutation (green), and also lead to change of surface potential from negative to positive. (c) The left panel shows wild-type Q447^{K10}, which forms hydrogen bonds with R450^{K10}. Q447P^{K10} mutation (green) disrupts these hydrogen bonds and the proline ring γ– and δ–carbons clash with N444^{K10} atoms (dashed lines), leading to helix kinking.

Fig. S13. Structural perturbations caused by Keratin 10 mutations I446T, Y449D, Y449C, R450P, and L453P. (a) The left panel shows wild-type Y449^{K10}, which forms stabilizing contacts with Y482^{K1}. Y449D^{K10} and Y449C^{K10} mutations (green) eliminate this stabilizing Tyr-Tyr contact, and the former also introduces negative surface potential. (b) R450P^{K10} mutation (green) eliminates positive surface charge and introduces a proline ring γ–carbon clash with the carbonyl oxygen (2.1 Å) of Q447^{K10} (dashed line), leading to helix 2B kinking. (c) In the top panel, wild-type L453^{K10} forms a major stabilizing hydrophobic interaction with L485^{K1}. L453P^{K10} mutation (green) disrupts this hydrophobic interaction and the proline ring δ–carbon clashes with the carbonyl oxygen (1.96 Å) of R450^{K10} (dashed line), leading to distal helix 2B kinking. (d) In the top panel, wild-type I446^{K10} forms multiple hydrophobic interactions with K1 (L475, E478, I479, Y482) and K10 (L442, Y449) residues, as well as hydrogen bond interaction with E443^{K10}. These interactions are disrupted with I446T^{K10} mutation (green).

Fig. S14. Assessing type of chemical change for human keratin mutations. All human keratin mutations (for K1, K5, K6a, K6b, K6c, K10, K14, K16, K17) documented in the Human Intermediate Filament Database were analyzed for the type of chemical change occurring and results for K5/K14 and K6a, K6b, K6c, K16, and K17 (keratins mutated in pachyonychia congenita) are summarized in panels (a) and (b). The most common type of change for K5/K14 was a hydrophobic residue to a hydrophobic residue (28%), and second most common was charged residue to a polar residue (19%). The most common type of change for pachyonychia congenita keratins was a hydrophobic residue to a hydrophobic residue (20%), and second most common was hydrophobic residue to a polar residue (19%). Definitions of residues were: acidic (D, E), basic (R, K), polar (Q, N, H, S, T, Y, C, G) and hydrophobic (A, I, L, F, V, P, M, W). (c) Raw data reporting the exact numbers of mutations for each type of chemical change across the keratins analyzed.